CHAPTER 4

HEXANARY AlCoCrFeNiMn HIGH-ENTROPY ALLOY

In this chapter, the phase evolution in mechanically alloyed hexanary AlCoCrFeNiMn high-entropy alloy is discussed in details. The alloy was divided into two ternary (AlCoCr & FeMnNi) systems to follow the sequential phase formation mechanisms. Thermal stability of the current alloy is followed by differential scanning calorimetry (DSC) and suitable annealing treatments. In addition, phase evolution after sintering is also analyzed and presented in the last section of the chapter.

4.1 Phase evolution

Fig. 4.1 shows the multiple displays of X-ray diffraction (XRD) patterns of AlCoCrFeNiMn high-entropy alloy powders after different milling hours. The diffraction peaks corresponding to all alloying elements can be predominantly observed in the initial blending of the powders, i.e. after 10 minutes of milling. After 5 hours of milling, diffraction intensities for all the elements decreases and the peaks tend to broaden. The intensity of the peaks corresponding to (111) plane of Al (d~2.32 Å), (311) plane of Al and (220) plane of Mn (d~1.21 Å) are reduced significantly after 5 h of milling. It has been found that diffraction peaks corresponding to Al disappear earlier than the other elements. Further increase in milling time up to 10 h suggests that most of the peaks lose their identity except Mn. This indicates that the formation of a solid solution by the dissolution of most of the element in the lattice of Fe or Cr. The identification of the host lattice is not quite straightforward at this stage, but it is obvious that it is close to BCC Fe &Cr. By increasing the milling time for next 5 h, it can be observed that there is no change in the position of the peak. However, the peaks can clearly be discerned to be

from a BCC lattice. Milling upto 20 h and above indicates the formation of the same BCC phase with the lattice parameter, which is higher than Fe but lower than Cr.

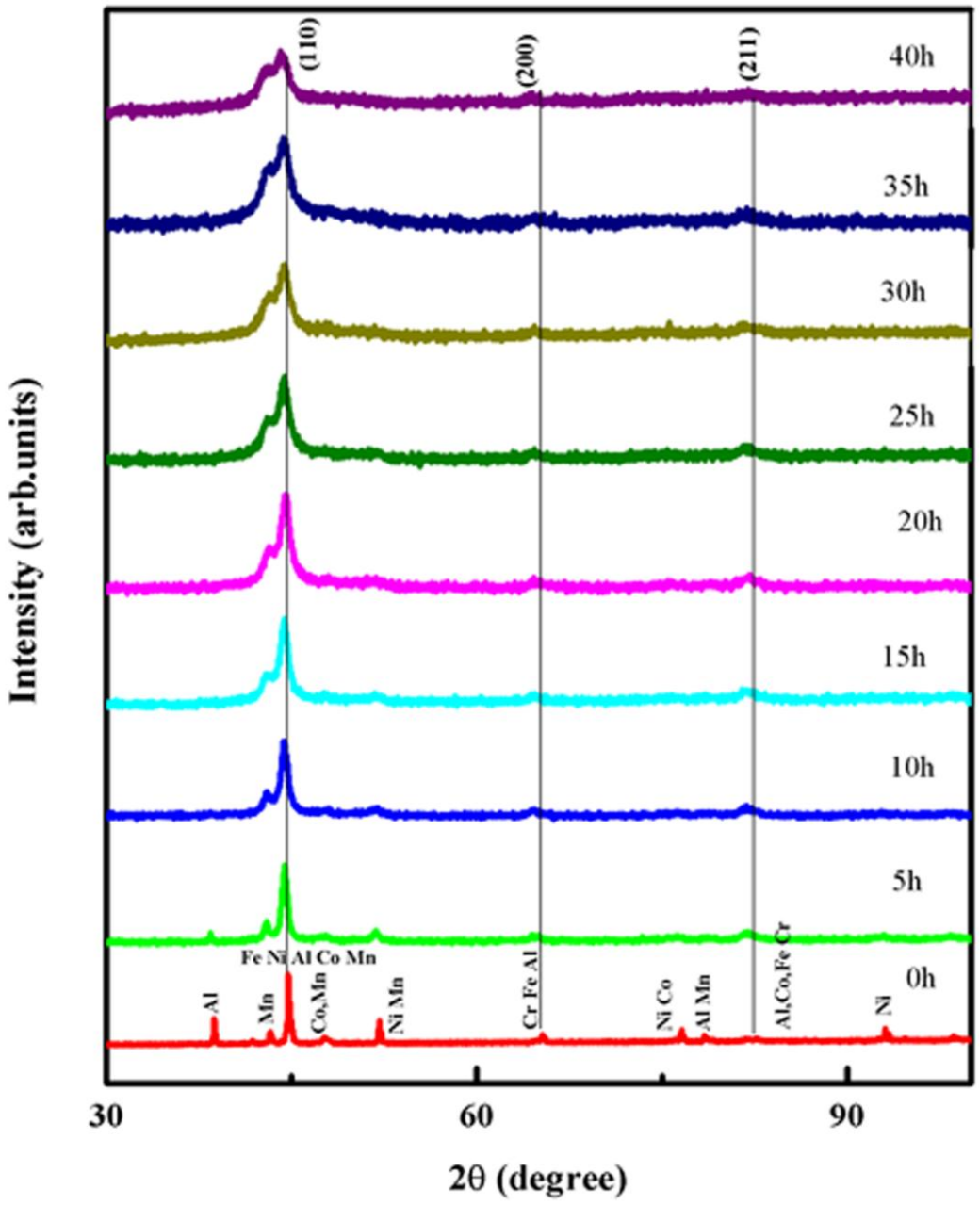

Figure 4.1: XRD patterns of AlCoCrFeNiMn HEA powders with different milling time. Evolution of the BCC phase is evident with the progress of milling.

The lattice parameter, as measured from the XRD pattern, turns out to be (a= 2.89 ± 0.02 Å). This indication becomes clearly evident on further increase in milling time up to 30h.

The XRD pattern of the 30h milled powder has a close agreement with a solid solution phase with the BCC structure. While analyzing the diffraction patterns with milling time, it has been found that the intensity decreases and broadening of the peaks take place. This was expected because of the reduced crystallize size and enhanced lattice strain (Table 4.1).

Table 4.1: The crystallite size and lattice strain of equiatomic AlCoCrFeNiMn high entropy alloy powder.

Milling time (h)	**5h**	**10h**	**15h**	**20h**	**25h**	**30h**	**35h**	**40h**
Crystallite size (nm)	20	18	17	17	16	15	15	15
Lattice strain (%)	0.54	0.61	0.63	0.66	0.67	0.68	0.69	0.70

This increase in lattice strain is mainly due to the introduction of elements in the host lattice of the high - entropy alloy and mechanical working of the powder during the mechanical alloying process. Although the complete solid solution was found to have formed at 30h of milling time, still milling was continued upto 40h in order to investigate any further phase transformation. However, no phase transformation could be detected. Hence it is clear that 40h milled powder shows the formation of a single-phase solid solution of a BCC structure with lattice parameter (a= 2.89±0.03Å). This solid solution formation may be the result of the high entropy effect of the alloying elements because all the alloying elements are in the equiatomic proportions. Here it is worthy to note that in AlCoCrFeNiMn high-entropy alloy system two elements (Fe, Cr) are having simple BCC structure and two (Al, Ni) having FCC along with one (Co) hexagonal structure (HCP). It may be mentioned that at room temperature, Mn is having a complex BCC structure similar to γ-brass structure. It is important to emphasize that the final high-entropy alloy

phase is a simple BCC in the structure of Fe or Cr type. It may appear that the phase selection of high-entropy alloy could be driven by the structure of a maximum number of constituent elements of high melting temperature. However, it may not often be always true. Wang et al. [139] have reported that Al stabilizes the FCC structure when it is less than 11at%, and it enhances the formation of BCC structure when it is present in more amounts. From the lattice parameter of the BCC phase, it can be assumed that the lattice of Fe is acting as the host lattice for this alloy system and the lattice parameter is slightly more than that of Fe and less than that of Cr. This result is also along the line of Hume-Rothery's rule of solid solution formation in binary alloy, which restricts the atomic radii difference between two constituent elements below 15 %. In AlCoCrFeNiMn high-entropy alloy, the average atomic size difference of elements is not more than 8 % what is actually proposed to be desirable for solid solution formation.

In order to understand the mechanism of solid solution phase formation, this hexanary alloy system was grouped into two (ternary) alloy systems. These alloy systems were taken on the basis of their milling behaviour during the hexanary alloy. AlCoCr and FeMnNi systems were separately milled upto 20 h and their milling behaviour with time was monitored by XRD. After that 20 h, milled powder from both the ternary alloys was mixed together and was milled further for another 20 h to observe the final phase formation. The evolution of phases in AlCoCr alloy system upto 20 h of milling as followed by XRD is given in Fig.4.2 (a). From this figure, all the elemental peaks of Al, Co &Cr are observed after 10 minutes of milling. However, with further milling initially Co peaks disappear, and the peaks get broadened due to the refinement of particle size and the introduction of strain. With further milling, some of the major peaks of Al also disappear finally leading to the formation of a BCC phase after 20 h of milling.

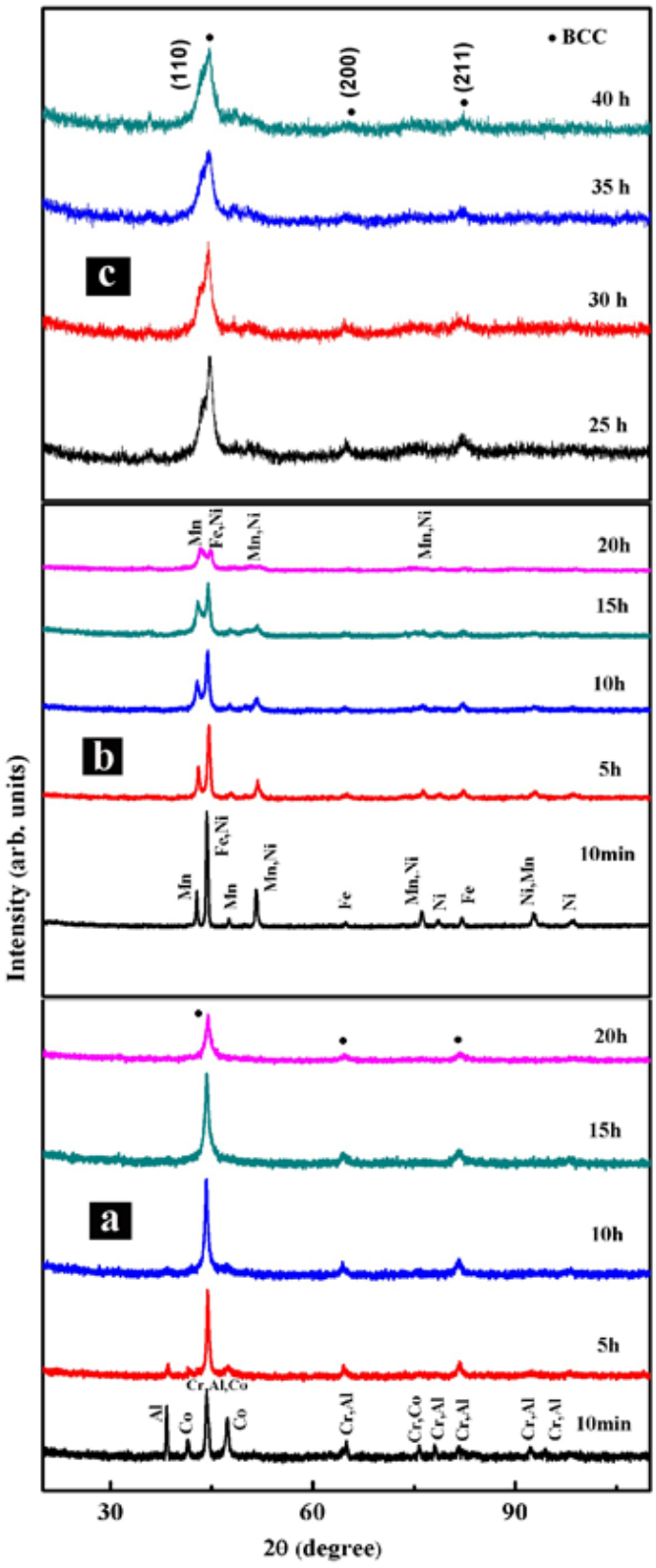

Figure 4.2: XRD patterns of (a) AlCoCr (b) FeMnNi (c) AlCoCrFeNiMn HEA powders with different milling time. In (a) after 20 hours of milling, no known phase appears. In (b) the phases cannot be ascertained and in (c) BCC phase appears after 25 hours of milling.

Milling behaviour of FeMnNi ternary alloy as followed by XRD is displayed in Fig.4.2 (b). In this system also individual elemental peaks of Fe, Ni and Mn are observed in the XRD pattern after 10 minutes of milling. In this alloy system, Mn peaks are the first to disappear or lose their identity. This necessarily means that Mn dissolves into another lattice first. Subsequently, some of the major peaks of Ni disappear and finally after 20 h of milling a phase evolves, the structure of which could not be ascertained. The phase evolution of mixed milled powder from the above two sets over next 20 h as followed by XRD is shown in Fig.4.2 (c). As observed from the XRD patterns, 5h of milling of the mixed powder leads to the formation of the BCC phase. Further milling does not lead to any change in the phase structure. However, the broadening of the peaks is evident. So from this study, it can be concluded that although mechanical alloying is a non-equilibrium process similar phase evolves after different milling sequence. It appears that phase evolution in this particular alloy system becomes path independent in the long run.

4.2 Analysis of powder morphology

Morphology of 40h milled alloy powder is provided in Fig. 4.3. It is observed that the particles are irregular in shape and their size varies in the range of 1-10 μm.

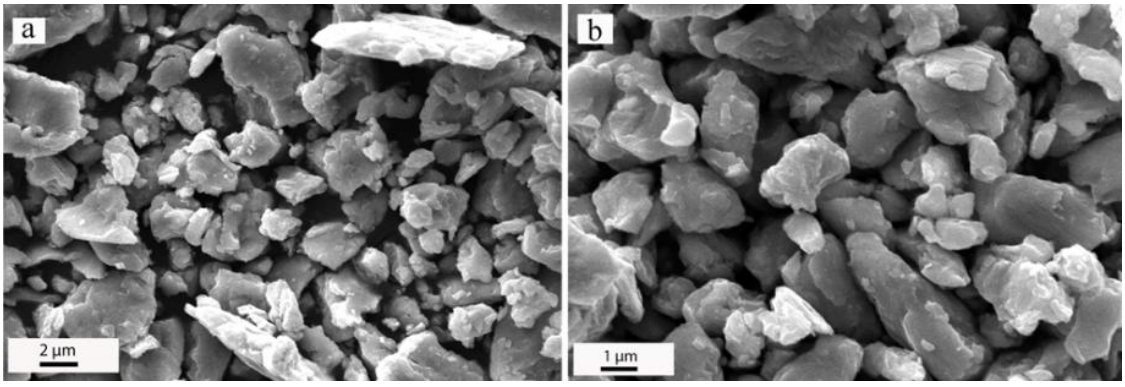

Figure 4.3: SEM micrographs of AlCoCrFeNiMn HEA powders with 40h of milling at different magnifications. In both cases, fractured particles with extensive river pattern on the surfaces can be observed.

Very often river-like flow patterns are observed on the particle surfaces, which have arisen due to the shear-type deformation and fracturing of the particles during the milling process. The size distribution of particles in the alloy is in the micron range and plot of this has been shown in the Fig.4.4.

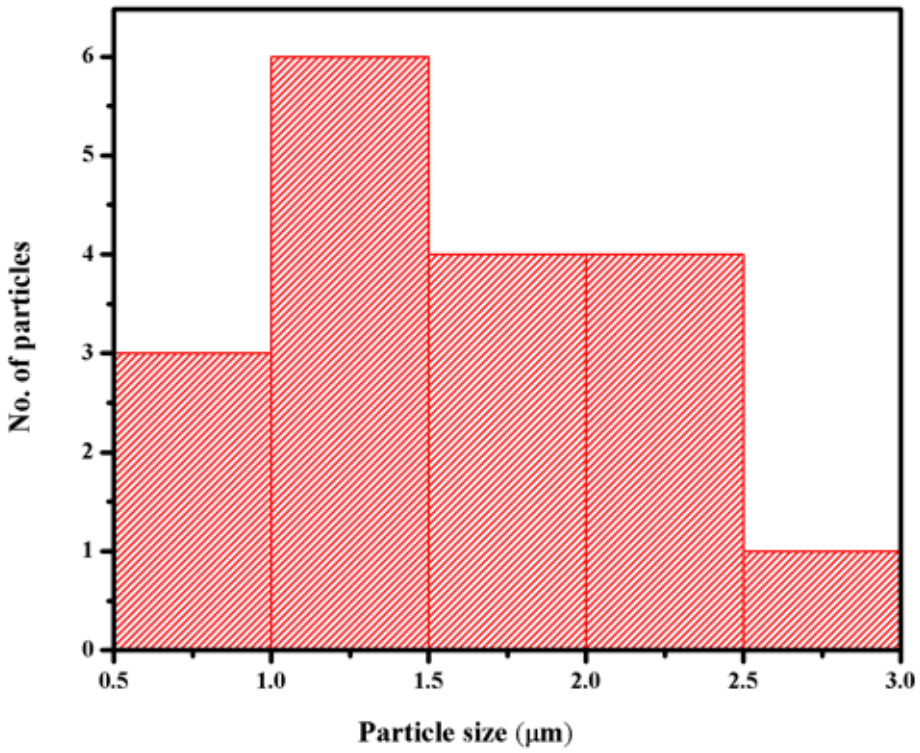

Figure 4.4: Particle size distribution in equiatomic AlCoCrFeNiMn high entropy alloy after 40 hours of milling. The median particle size is in the range ~ 1-1.5 μm.

In doing the particle size measurement, absolute measurement technique was adopted, i.e. the particle size was measured directly from the micrograph, and the largest dimension was taken as the particle size.

4.3 Nanostrcured nature and elemental mapping of mechanically alloyed powder

The presence of the phases and their alloying effects has been studied in a detailed manner through the transmission electron microscopy (TEM). A bright-field images and the corresponding SAD pattern have been shown in Fig. 4.5 (a) and 4.5 (b)

respectively. The formation of ring patterns in the SAD pattern indicates the alloy particles are closely random oriented. Indexing of these ring patterns confirms that a single BCC phase (a= 2.91±0.02 Å) is present in the 40 h milled AlCoCrFeNiMn high entropy alloy powder. Additionally, the d-spacings corresponding to these rings are matching closely with those observed in the X-ray diffraction patterns.

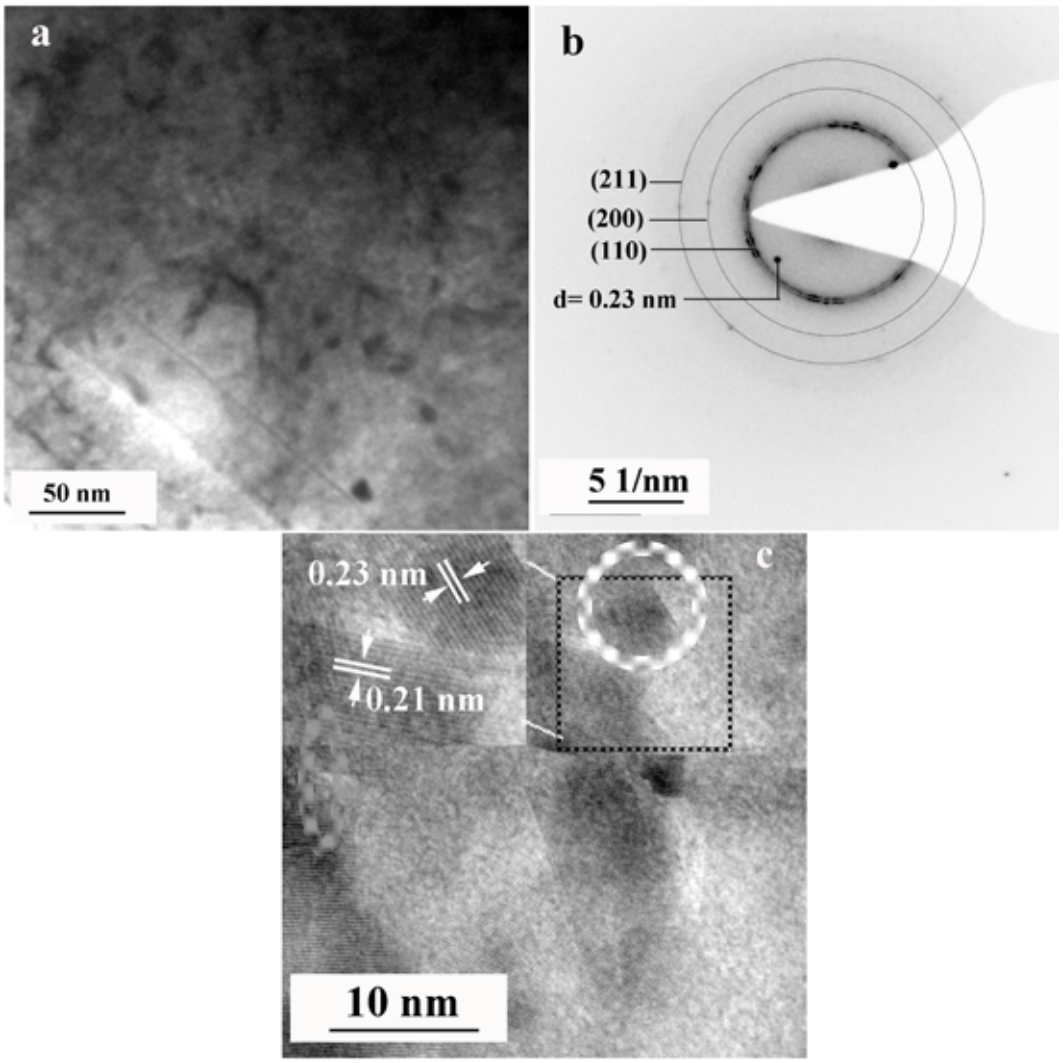

Figure 4.5: TEM bright-field image (a) of 40h milled AlCoCrFeNiMn HEA powder and corresponding SAD pattern (b) with HRTEM (c). From the diffraction pattern, the presence of the BCC phase can be confirmed. Similar spacings are observed in the high-resolution image also.

There are two intense spots in the SAD pattern corresponding to 2.36 Å. It does not match with any known d-spacing of any of the constituent elements, neither this peak was observed in the x-ray diffraction pattern.

A careful investigation reveals that this d-spacing corresponds to Cr_2O_3 (110) and Al_2O_3 (110). Fig.4.5 (c) shows the high-resolution image (HRTEM) of the 40 h milled high entropy alloy powder. In the image, lattice fringes corresponding to the alloy is observed in multiple directions. The random orientation of the particles and lattice fringes further confirms the origin of regular ring pattern in the diffraction pattern. In addition to that, the particles are faceted which, might have originated from the fracturing of the particles during mechanical alloying. Due to the presence of different elements in the lattice, the lattice planes are expected to be distorted. The lattice fringe corresponding to the oxide is also observed in the high-resolution image. The regions where lattice fringes are disappearing are the regions where fracturing took place, and it is along a definite plane due to the huge amount of micro strain present in the alloy. This large amount of micro strain is due to the mechanical alloying and addition of elements in the high-entropy alloys. Inter-planar spacing from these lattice fringes is 2.36 Å, which closely matches with the Cr_2O_3 (110), and 2.11 Å correspond to (110) plane of the BCC phase.

The STEM-EDS elemental mapping of the 40 h milled powder sample has been shown in Fig.4.6. It has been found from the elemental mapping that all the elements of the hexanary alloy are distributed uniformly. There is no signature of heterogeneity. This confirms that all the constituent elements are incorporated in the host lattice to give rise to the high entropy alloy. However, a detailed look at the elemental maps indicates that a minor variation in intensity is present in the maps. As the alloyed particles are repeatedly fractured, their shapes are not uniform, and considerable variation in thickness also exists.

Pertaining to these two factors, interaction volume of the electron beam with the particles changes and X-ray signal generation also undergoes changes locally, which might have led to the variation in intensity.

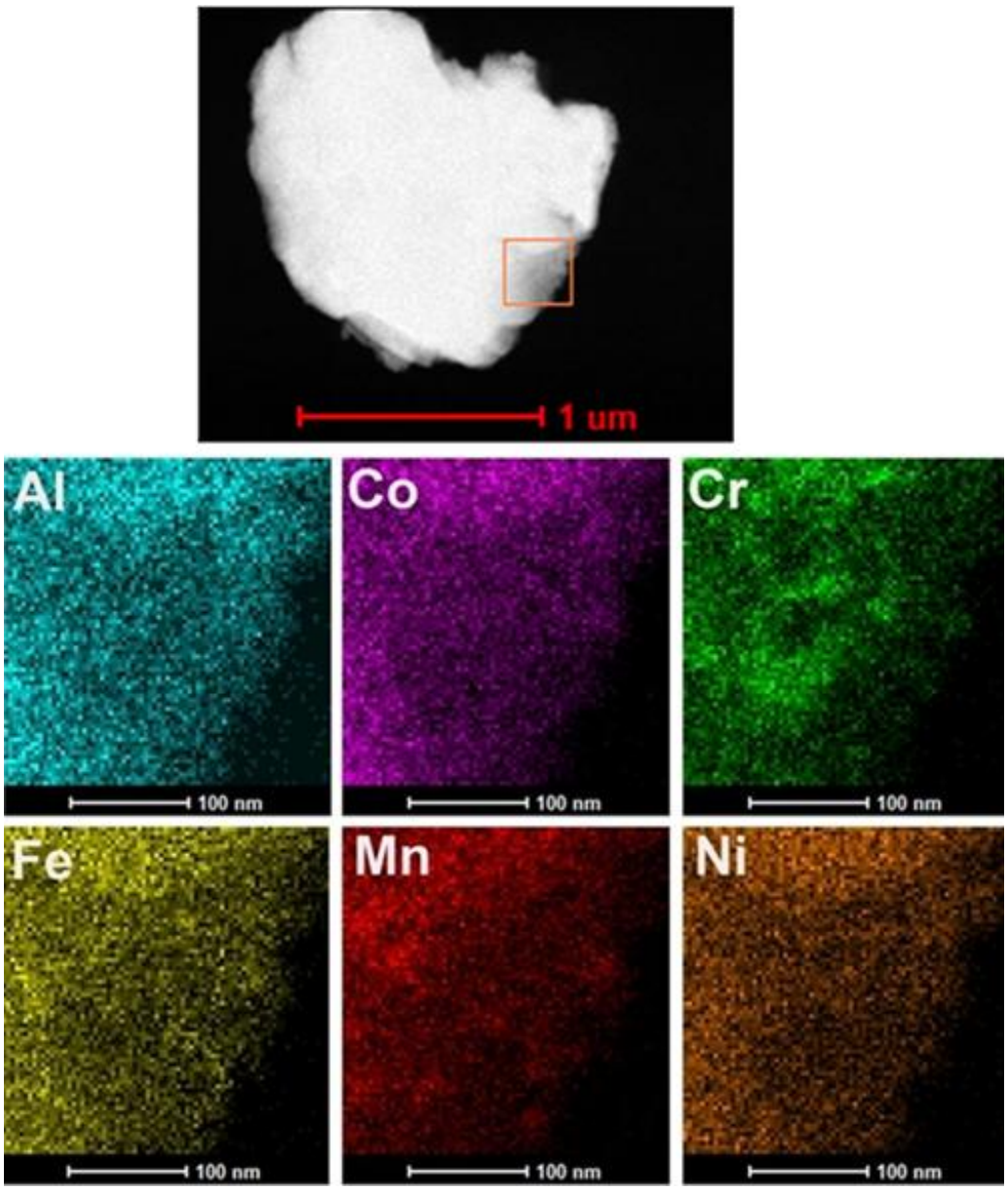

Figure 4.6: The STEM-EDS mapping of equiatomic AlCoCrFeNiMn hexanary high-entropy alloy after 40h of milling. The elements are homogeneously distributed to give rise to the single BCC phase.

4.4 Thermal stability

Thermal stability of the 40h milled high entropy alloy has been investigated through dynamic DSC at different heating rates (10, 20, 40 & 50 K/min) and corresponding thermograms are shown in Fig. 4.7. Eventhough similar thermal events are seen in all the thermograms, their intensity varies. At the higher heating rate, two exothermic heat events are observed. However, at a lower heating rate, the higher temperature heat event is absent.

Additionally, the intensity of the first heat event (exothermic in nature) decreases with the decrease in the heating rate. This is due to the fact that the transformations corresponding to these heat events are diffusive in nature, and they are not so sensitive to the characteristic temperature. At a lower heating rate, as long incubation or residence time is available, the transformation starts at lower temperature itself, which leads to the reduction in heat evolution at the characteristic temperature. In a similar line, it could be argued as to why the higher temperature heat events are missing in the thermograms with lower heating rates. With higher heating rates, due to the unavailability of enough residence time, the heat events are much more pronounced. It is important to mention that the heat events at higher heating rates gradually transfer to the higher temperature side due to the diffusive nature of the transformation processes. The second heat event that appears at 40 K/min heating rate is not so clearly visible at 50 K/min heating rate, probably due to its shift to a higher temperature. However, the transformation related to this heat event is real that is confirmed by ex-situ heat treatment and subsequent structural characterization, which has been reported in the following sections.

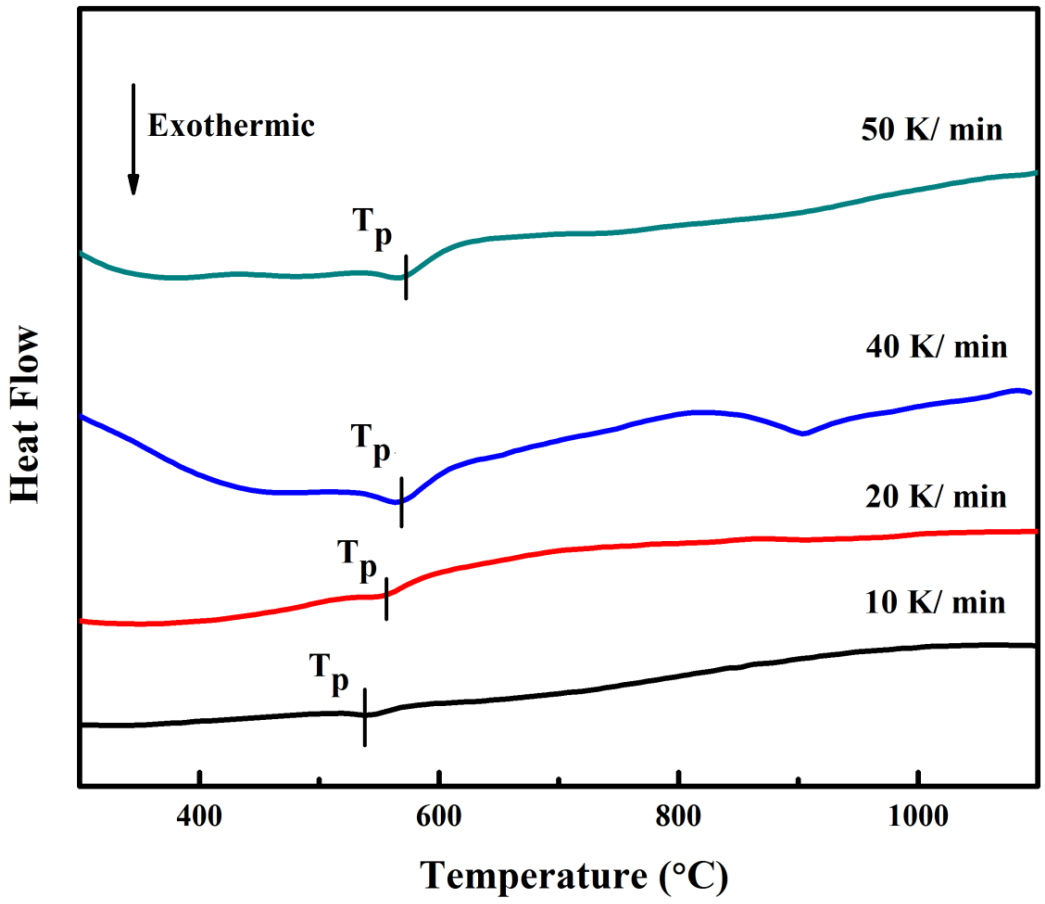

Figure 4.7: DSC thermogram of 40h milled AlCoCrFeNiMn high entropy alloy powder at different heating rates. Two exothermic heat events are observed at higher heating rates, which are reduced to one heat event at lower heating rates, which may be attributed to the diffusional nature of the transformation process.

Activation energy calculation for the transformation of this alloy has been done through Kissinger and Ozawa models [140,141]. Plots were drawn using these equations:-

$$\ln\left(\frac{\beta}{T_P^2}\right) = -\frac{E}{RT_p} + c_1 \text{(Kissinger equation)} \quad \ldots\ldots\ldots\ldots\ldots\ldots \text{(4.1)}$$

$$\ln(\beta) = -\frac{E}{RT_p} + c_1 \text{(Ozawa equation)} \quad \ldots\ldots\ldots\ldots\ldots\ldots\ldots \text{(4.2)}$$

From the slope and the intercept of the straight line, it is possible to calculate the activation energy of transformation for both the equations. Here β is the heating rate in K/min, T_p is the peak temperature (Kelvin), R is the universal gas constant, and E is the

activation energy. All the relevant data and activation energies have been shown in Table 4.2. The activation energy of the second heat event was not possible to be calculated as the peak was not observed at lower heating rates. The activation energies for the first heat event by Kissinger method and by Ozawa method turn out to be 310 and 324 kJ/mol respectively. Given the assumptions of these models, the values are quite close and corroborating.

Table 4.2: Activation energies calculation by Kissinger and Ozawa model for the first transformation event of the AlCoCrFeNiMn high entropy alloy.

Heating Rate (β), K/min	**Peak Temperature (K)**	**Activation Energies kJ/mol-K**	
10	814	310 (Kissinger model)	324 (Ozawa model)
20	822		
40	838		
50	840		

.

In order to understand the phase transformations associated with the heat events as observed in DSC, high-temperature in-situ XRD was conducted of this 40 h milled powder sample at seven different temperatures form 350 (623 K) to 800 ºC (1073 K) at regular interval of 75 ºC (346 K).XRD patterns as obtained at all these temperatures have been shown in Fig.4.8 & 4.9. Fig. 4.8 consists of the X-ray diffraction patterns as obtained upto 500 ºC (773 K) and Fig. 4.9 contains the patterns as obtained above 500 ºC (773 K). From XRD plot, it can be seen that there was no change in the phase upto 500 ºC (773 K), it means that this alloy is stable upto this temperature for the said interval of time. Detailed analysis of the peak positions of all the XRD patterns has been done. It has been found that at 575ºC (K) nucleation of $Mn_3Co_7$and $L1_2$ type Ni_3Al phase along with the retained BCC phase takes place. Further analysis of the diffraction patterns corroborates these phenomena in the same line upto 650 ºC (923 K). It is interesting to

observe that at 725 ºC (998 K) a FCC phase appears along with the other retained phases. This FCC phase (a= 3.63 ±0.02Å) also has a strong proximity with $L1_2$ type Ni_3Al (a= 3.67±0.03Å) phase.

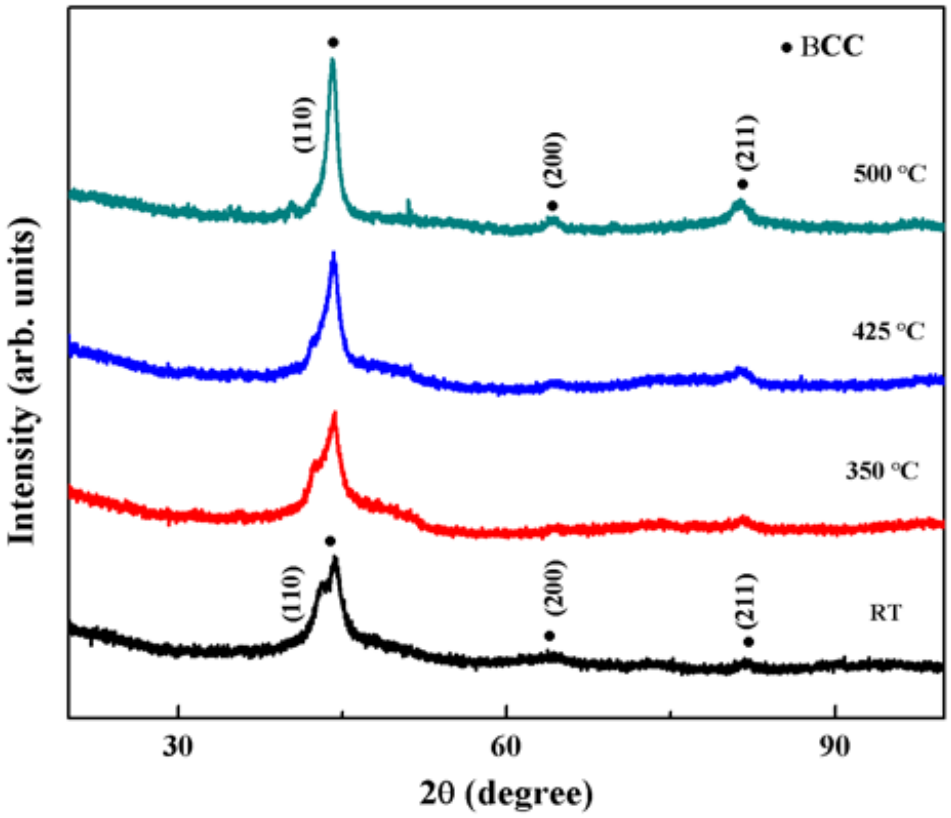

Figure 4.8: XRD patterns 40h milled AlCoCrFeNiMn high entropy alloy powder upto 500 ºC (773 K). No phase transformation is observed up to this temperature, which signifies that the alloy is stable up to this temperature.

It has been observed from the thermal stability study and nature of phase evolution that the transformation through which the alloy changes its phase constituent and microstructure is diffusive in nature. Pertaining to this behaviour, it is difficult to assign a singular and accurate temperature for thermal stability. The thermal stability temperature quoted above should be taken as a ballpark value. In the X-ray diffraction pattern after heat treatment at 500 °C small peaks of the second phase could be observed. The

intensity of those peaks being small; it has been considered that the volume fraction of those phases is relatively small to introduce any significant change in the microstructure.

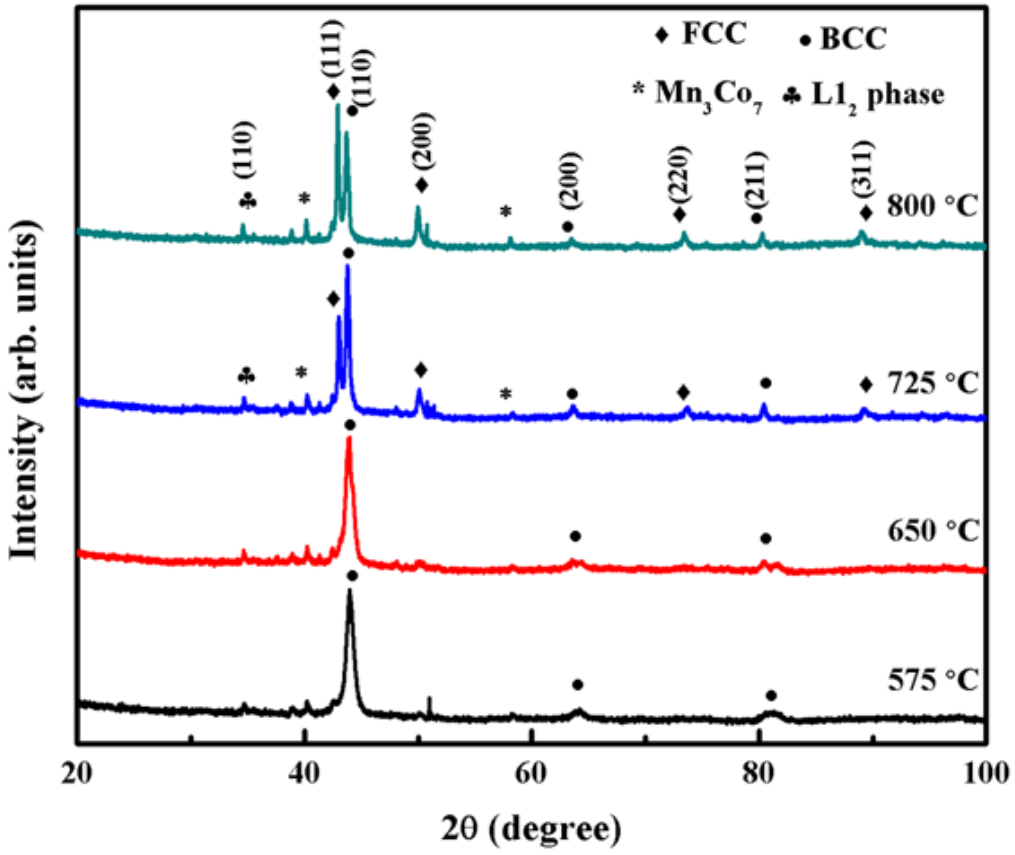

Figure 4.9: XRD pattern 40h milled AlCoCrFeNiMn high entropy alloy powder upto 800ºC (1073 K). Sequential precipitation of $L1_2$ phase and Mn_3Co_7 phases are clearly observed.

To understand thermal stability, the high entropy alloy samples annealed at 500 ºC (773 K) and 800 ºC (1073 K) were observed in TEM. Bright-field images with corresponding diffraction patterns of these samples have been shown in Fig. 4.10 &4.11. The bright-field image of the alloy heat-treated at 500 ºC (773 K) (Fig.4.10) reveals the fine-grained structure of the alloy in which grains are irregular in shape, and their size ranges between 5-10 nm. In the diffraction pattern, also the rings corresponding to the BCC phase is obtained. This further proves that the alloy is thermally stable upto 500 ºC (773 K). The bright-field image of the alloy after heat treatment at 800 ºC (1073 K) (Fig. 4.11) shows

two types of polygonal grains, which are basically different in their size. One type of grains, which are mostly distributed all over the matrix and they arein size range of 50-100 nm.

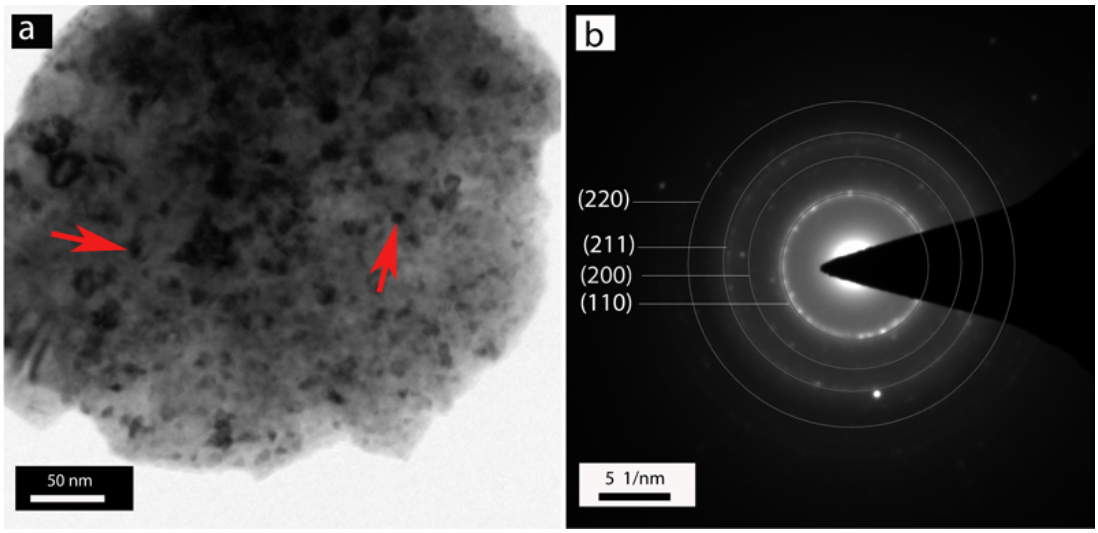

Figure 4.10: Bright field image and corresponding SADP of AlCoCrFeNiMn powder sintered at 500 ºC (773 K) under control atmosphere. Fine-grained structure (shown with arrows) of the alloy and the presence of the BCC phase is observed after sintering.

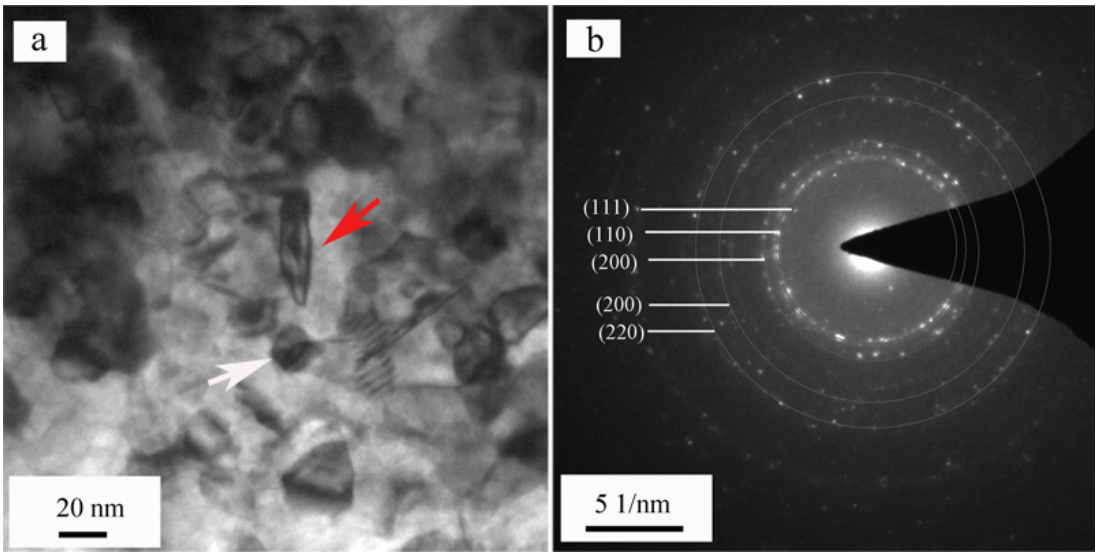

Figure 4.11: (a) Bright-field image and (b) corresponding SADP of AlCoCrFeNiMn powder sintered at 800ºC (1073 K) under control atmosphere. The grains are faceted (shown with arrows) however not extraordinarily grown due to sluggish diffusion kinetics.

The other type of grains, which is scattered in the matrix and is in size range of 15-30 nm. In the diffraction patterns, the signature of the BCC phase, as well as the FCC phase, could be ascertained.

4.5 Microstructural characterization and phase evolution of sintered alloy

Visible light micrographs of microwave sintered AlCoCrFeNiMn high entropy alloy, which were sintered at 900 (1173 K), 950 (1223 K) & 1000 ºC (1273 K) are shown in Fig. 4.12.

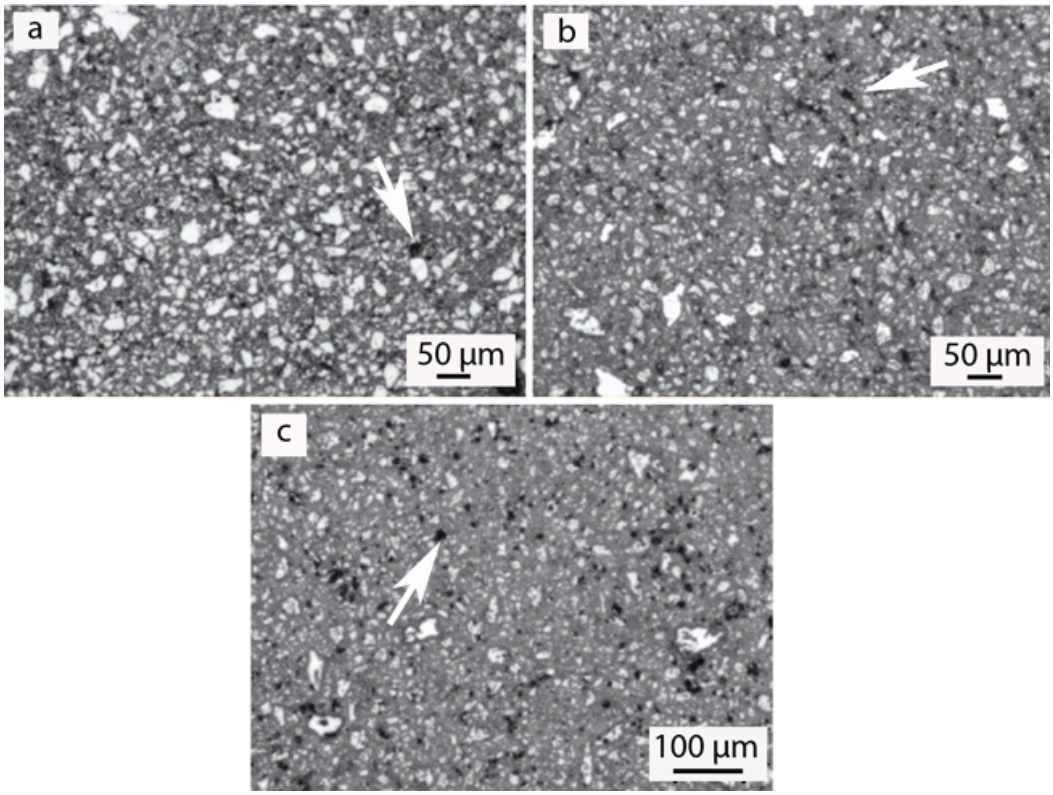

Figure 4.12: Optical micrographs of AlCoCrFeNiMn HEA compact after microwave sintering at (a) 900 (1173 K) (b) 950 (1223 K) (c) 1000 ºC (1273K). Fine distribution of grains and porosity (shown with arrows) can be observed.

From micrographs, it can be seen that as the temperature of sintering increases the coarsening of the grains increases. In the same line, porosity (shown with arrows) of the sample also decreases, which can be observed. XRD patterns of the alloy microwave

sintered at 900 ºC (1173 K), 950 ºC (1223 K) & 1000 ºC (1273 K) have been shown in Fig. 4.13. It is evident that along with the BCC phase nucleation of an ordered Ni_3Al type intermetallic phase takes place.

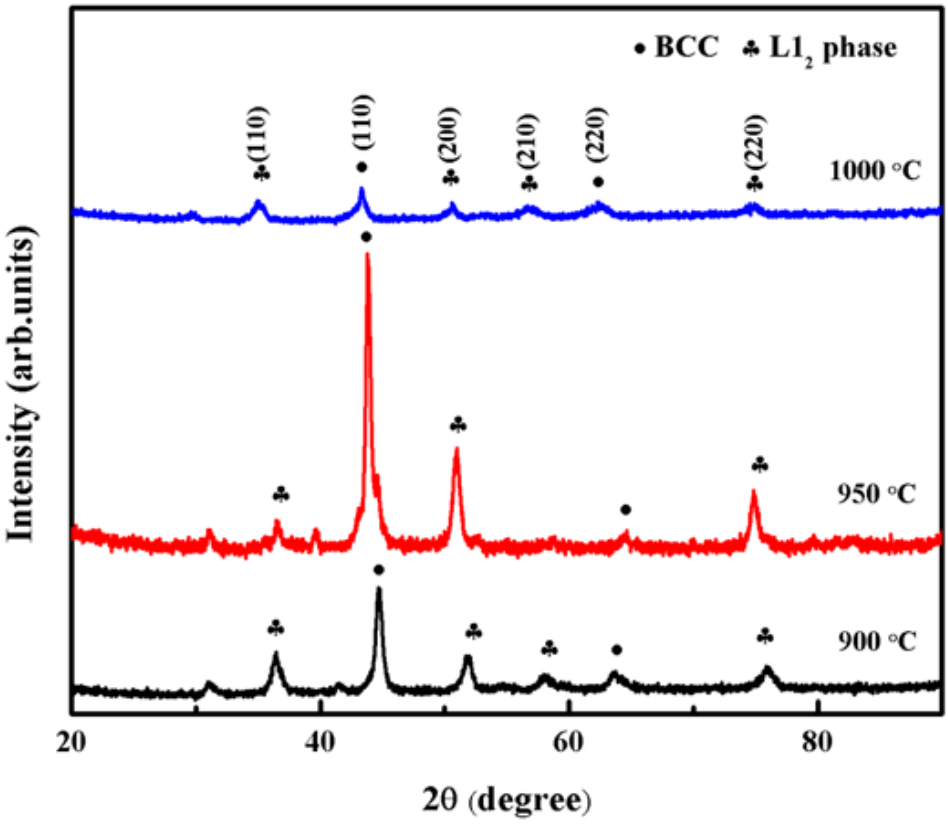

Figure 4.13: XRD patterns of AlCoCrFeNiMn HEA alloy compact after microwave sintering at 900 (1173 K), 950 (1223 K) & 1000ºC (1273K). Along with the BCC phase, the presence of $L1_2$ phase can also be discerned.

4.6 Discussion

The discovery of high entropy alloys began almost at the same time as that of bulk metallic glass-forming alloys [1]. However, the scientific community took a serious interest in exploring and understanding the nuances of alloy design in this category, little more than a decade later [12]. A peek into the alloy design strategies for high-entropy alloys reveals that there are quite a few similarities in these two alloy systems [34]. For

bulk metallic glass formation, the atomic size difference is prescribed to be more than 15% leading to structural frustration in the crystal which is just the opposite to what has been prescribed for high entropy alloys. In the case of high-entropy alloys, the atomic size difference less than 15% basically favours substitutional solid solution formation. While the atomic size mismatch criteria for bulk metallic glass formation may be considered as opposite to Hume-Rothery rule for solid solution formation, the same for high entropy alloys may be seen as the proHume-Rothery rule.The atomic size difference among all the elements of AlCoCrFeMnNi alloy is given in Table 4.3. It is observed that none of the differences is above 15%.

Table 4.3: The values of atomic size difference δ (%) in the AlCoCrFeNiMn high entropy alloys system.

Element	Al	Co	Cr	Fe	Ni	Mn
Al	-	6.7	6.8	7.1	6.9	2.9
Co	6.7	-	0.08	0.4	0.2	3.8
Cr	6.8	0.08	-	0.32	0.12	3.9
Fe	7.1	0.4	0.32	-	0.20	4.2
Ni	6.9	0.2	0.12	0.20	-	4.0
Mn	2.9	3.8	3.9	4.2	4.0	-

The second level of difference that exists is the restriction on composition in case of high-entropy alloys. It is recommended to be within 5-35 at%. No such guideline exists for bulk metallic glass-forming alloys. However, bulk metallic glasses with equiatomic or almost equiatomic composition has been reported in the literature **[**142]. Additionally, for bulk metallic glasses, it has been recommended that the binary enthalpies of mixing should be highly negative that favours intermetallic phase formation. In stark contrast to that, it has been reported that in high-entropy alloys, the entropy of mixing should play an important role. Hence entropy should be considered in order to assess the stability and

formation of high-entropy alloys. As intermetallic based high-entropy alloys have also been reported, it is a challenge to establish semiempirical thermodynamic criteria to predict the stability of high entropy alloys. In a remarkable advancement in that direction, Zhang et al. [35] have reported that the ratio between $T\Delta S_{mix}$ and ΔH_{mix} should be taken into consideration. They have shown that in the ratio of high-entropy alloy forming systems, it is always more thanone, whereas the same for the bulk metallic glass-forming alloys is less than 1.The binary heats of mixing of several components in AlCoCrFeNiMn are given in Table 4.4. This binary enthalpy of mixing are calculated on the basis of Miedema macroscopic model [38].

Table 4.4: The values of chemical enthalpy of mixing (ΔH_{ij}^{mix}, kJ/mol), of atomic pairs for AlCoCrFeMnNi high entropy alloy, following the Miedema's approach.

Element	Al	Co	Cr	Fe	Ni	Mn
Al	-	-19	-10	-11	-22	-19
Co	-19	-	- 4	-1	0	-5
Cr	- 10	- 4	-	-1	-7	2
Fe	- 11	- 1	- 1	-	-2	0
Ni	- 22	0	- 7	- 2	-	-8
Mn	-19	- 5	2	0	- 8	-

It is observed from the table that none of the binary heats of mixing is positive, which necessarily indicates that there should not be any likely tendency for phase separation. Moreover, the heats of mixing values are negative, however small. The only high negative enthalpy of mixing is observed in Al-Ni, Al-Co and Al-Mn systems, which are reported in Table 4.4. In these systems, quite a few intermetallic phases are observed. Basu and Ranganathan [143] earlier reported through a series of phase diagram search that a number of intermetallic phases are somehow empirically related to the heat of mixing. This alloy system is also not an exception to that. For the present alloy system T_m, ΔS_{mix} and ΔH_{mix} (chapter 1) are calculated and reported in Table 4.5.

Table 4.5: Calculated thermodynamic parameters for AlCoCrFeMnNi high entropy alloy

ΔH_{mix} (kJ/mol)	T_m (K)	ΔS_{conf} (J/mol-K)	Ω
-11.39	1944	14.89	2.5

It has been observed that the ratio, as proposed by Zhang et al. [35] turns out to be 2.5 for this alloy system. This is very much in the range as proposed in the earlier literature. The discussion above brings out clearly the difference of this alloy system with bulk metallic glass-forming alloys and its suitability as a high entropy alloy.

4.6.1 Mechanical alloying behaviour

In the present work, the alloy system was mechanically milled, and the evolution of phases was monitored with a specific time interval. It has been observed that the Al, Co and Mn peaks disappear sequentially. It has been understood that the elements with lower melting point lose their identity first [144]. In the present case Al, along with Co &Mn gets dissolved and Fe, Cr retains its identity. Based on this observation, it can be concluded that the melting point criteria might be system-specific or at least does not hold good universally. Further, we would like to note that dissolution criteria based on melting point is partially based on empiricism, and there are other factors, which might change the dissolution behavior. Moreover, disappearance or reduction of the intensity of certain peaks of an element in XRD may be the effect of various other factors relating to the scattering behavior of that particular element. A definitive conclusion needs further work and close sensitivity of the milling behavior. This issue is worth pursuing for better understanding. As the milling time increases peaks intensity decreases with an increase in broadening. This is expected because the increase in milling time decreases the

crystallite size and increases the lattice strain. The complete formation of the solid solution phase has been found after the 30 h of milling. Milling was further increased up to 40 h to investigate any phase transformation, but it does not exhibit any change. The earlier report shows that similar phases are present even after 60 h of milling [106]. This necessarily means that after 30 h of milling no further change in the structure of this alloy takes place and this excess hour of milling is basically redundant so far the phase evolution in this alloy is concerned. The 40h milled sample showed the single-phase solid solution of BCC crystal structure, which was confirmed through XRD and TEM study. In an earlier study [106], it has been reported that a FCC phase along with the BCC phase appears after completion of milling though in minor quantities. In the present case, rigorous analysis of the diffraction patterns does not confirm any presence of FCC phase. High-resolution phase contrast images from the milled powder reveal the lattice structure of the BCC phase. The lattice plane corresponding to the BCC phase has also been resolved. However, occasionally a lattice fringe has been resolved which does not match with the BCC phase. The fringe spacings match with the oxide of aluminium. As the milling was carried out in an inert atmosphere, the possibility of forming an oxide phase even in minor quantities cannot be ruled out. However, the powder was dried in the air, which could have resulted in minor oxide phase formation. In any case, this cannot be related to the phase structure of the alloy. In a similar line, carbide formation has been reported in wet milling and/or after subsequent heat treatment. In the case of carbide formation, corresponding diffraction peaks are observed in X-ray and electron diffraction patterns. Moreover, predominant contrast enhancement in STEM-EDS maps is also observed in localized regions. In the present study, none of the above-mentioned features could be observed, which rules out the possibility of extended carbon contamination and carbide formation [145]. In order to further understand the solid solution phase formation

mechanism of this hexanary alloy, the alloy was divided into two ternary alloy systems. These two ternary alloy systems (AlCoCr and FeMnNi) were milled for up to 20 h in the separate vials. After the 20 h of milling these two systems were mixed together and the mixed powder was milled for further 20 h. This new way of milling of high-entropy alloy system shows the same phase as was found in the single hexanary alloys system. From this study, it can be deduced that although the mechanical alloying is the non-equilibrium process, it evolves the same phase and independent of the processing route for this particular alloy system.

4.6.2 Thermal stability

In the dynamic differential scanning calorimetric thermogram, it has been observed that phase composition of the alloy changes in two separate exothermic heat events when it is heated upto 1100 ºC (1373 K). The alloy is stable upto 500 ºC (773 K), andsubsequently, the heat events appear at around 540 ºC (813 K) and 900 ºC (1173 K). It is important to note that the peak temperatures for these heat events shift to the right as the heating rate is increased. In addition to that, the heat evolved at each event is increased as the heating rate is increased. These observations can be explained in the light of diffusional transformation. Similar behaviour is observed in the glasses and other metastable alloys when they undergo a diffusional transformation [146,147]. As the diffusional transformation has a characteristics incubation time as the heating rate increases the peak shifts to the higher temperature side.Moreover, at lower heating rates as more of residence time is available, the diffusional transformation starts beforehand leading to a decrease in the heat evolution at the peak temperature. The activation energies calculated based on two different models corroborate well. Though published

literature does not exist on this particular transformation, activation energies for transformation in glasses and metastable alloys lie in this range only.

The phases evolved with the heat events have been explored through in-situ high-temperature XRD and TEM. It is observed that a FCC phase, which is quite closely related to the Ni_3Al phase, evolves after the first transformation event. After the second transformation, Mn_3Co_7 phase could be observed in the alloy. The evolution of this phase after heat treatment has been reported in the earlier literature [106]. As a result of the evolution of these phases, the high entropy alloy matrix should become richer in the remaining elements. Transmission electron microscopy reveals that the phases are nanocrystalline. It is likely to happen as the alloy is multi-component; the diffusion of the elements leading to the transformation is likely to be sluggish. Similar, phase evolution has been observed after sintering also.

4.7 Conclusions

The following conclusions are drawn from this chapter-

1. AlCoCrFeNiMn equiatomic alloy leads to the formation of single-phase BCC (a= 2.89±0.03Å), alloy upon mechanical alloying. Similar phase evolution is obtained by dividing the alloy composition into two different segments and milling them in a different schedule.
2. The semi-empirical thermodynamic analysis reveals that the ratio of $T\Delta S/\Delta H$ is ~2.5, which is well within the range of high entropy alloys as reported in the literature.
3. The high entropy alloy is stable upto ~500 ºC (773 K), and then it undergoes two diffusional transformations leading to the precipitation of a nanocrystalline FCC

ordered phase (a= 3.63 ±0.02Å) closely related to Ni_3Al type intermetallic phase with subsequent precipitation of minor amount of Mn_3Co_7 phase.

4. Consolidated and sintered pellet of the same alloy after heat treatment shows the precipitation of similar phases, as observed in heat-treated samples.